# Prediction of two-dimensional nodal-line semimetal in a carbon nitride covalent network

| | |
|---|---|
| Journal: | *Journal of Materials Chemistry A* |
| Manuscript ID | TA-ART-03-2018-002555.R2 |
| Article Type: | Paper |
| Date Submitted by the Author: | 29-Apr-2018 |
| Complete List of Authors: | Chen, Haiyuan; Institute of Fundamental and Frontier Sciences and School of Materials and Energy, University of Electronic Science and Technology of China, Chengdu 610054, P R China<br>Zhang, Shunhong ; Institute for Advanced Study, Tsinghua Unviersity, Beijing 100084, PR China<br>Jiang, Wei; Department of Materials Science and Engineering, University of Utah, Salt Lake City, UT 84112, USA<br>Zhang, Chunxiao ; Department of Materials Science and Engineering, University of Utah, Salt Lake City, UT 84112, USA<br>Guo, Heng; University of Electronic Science and Technology of China, State Key Laboratory of Electronic Thin Film and Integrated Devices<br>Liu, Zheng; Tsinghua University<br>Wang, Zhiming; University of Electronic Science and Technology of China,<br>Liu, Feng; University of Utah, Department of Materials Science<br>Niu, Xiaobin; University of Electronic Science and Technology of China, State Key Laboratory of Electronic Thin Film and Integrated Devices |
| | |

# Prediction of two-dimensional nodal-line semimetal in a carbon nitride covalent network

**Haiyuan Chen,[ab] Shunhong Zhang,[cb] Wei Jiang,[b] Chunxiao Zhang,[b] Heng Guo,[a] Zheng Liu,[cd] Zhiming Wang,[a] Feng Liu, [*bd] and Xiaobin Niu[*a]**

[a] Institute of Fundamental and Frontier Sciences and School of Materials and Energy, University of Electronic Science and Technology of China, Chengdu 610054, P. R. China

[b] Department of Materials Science and Engineering, University of Utah, Salt Lake City, UT 84112, USA

[c] Institute for Advanced Study, Tsinghua University, Beijing 100084, P. R. China

[d] Collaborative Innovation Center of Quantum Matter, Beijing 100084, P. R. China

Corresponding author: xbniu@uestc.edu.cn, fliu@eng.utah.edu

## Abstract

Carbon nitride covalent compounds have emerged as a prominent member of 2D materials beyond graphene. The experimental realizations of 2D graphitic carbon nitride g-$C_3N_4$, nitrogenated holey grahpene $C_2N$, polyaniline $C_3N$ have shown their promising potential in energy and environmental applications. In this work, we predict a new type of carbon nitride network with a $C_9N_4$ stoichiometry from first principle calculations. Unlike common C-N compounds and covalent organic frameworks (COFs), which are typically insulating, surprisingly $C_9N_4$ is found to be a 2D nodal-line semimetal. The nodal line in $C_9N_4$ forms a closed ring centered at Γ point, which originates from the $p_z$ orbitals of both C and N. The linear crossing happens right at Fermi level contributed by two sets of dispersive Kagome and Dirac bands, which is robust due to negligible spin-orbit coupling in C and N. Furthermore, it is revealed that the degeneracy along the high-symmetry path is protected by out-of-plane mirror or $C_2$ rotation symmetry, rather than in-plane mirror symmetry. The chemical potential difference of C and N, as validated by a single orbital tight-binding model, plays a significant role in forming the nodal ring. Interestingly, a new structure of nodal line, i.e., nodal cylinder, is found in momentum space for AA-stacking $C_9N_4$. Our results imply possible functionalization for a novel metal-free C-N covalent network with interesting semimetallic properties.

**Keywords: nodal-line semimetal, carbon nitride, covalent organic framework, nodal cylinder, first-principles calculations**

## Introduction

Graphene[1] discovered in 2004 has fostered a new research filed of two-dimensional (2D) materials, attracting continued research attention. Much effort has been devoted to searching for new 2D materials beyond graphene. Next to C in the periodic table, N appears to be a suitable partner to compose another important set of 2D materials with C. The 2D polyaniline with a $C_3N$ stoichiometry has been successfully synthesized by a direct pyrolysis of hexaaminobenzene (HAB) trihydrochloride single crystals very recently.[2] The $C_3N$ monolayer can be considered as N-substituted graphene with uniformly distributed N atoms in an ordered pattern, which possesses an indirect band gap.[3] This C-N compound not only has great potential for applications in nano-electronics but also as a functional unit.[4-6] In comparison with the hole-free honeycomb $C_3N$ monolayer, the holey generated C-N covalent networks [7-12] also draw a great deal of interest lately. Graphitic carbon nitride, g-$C_3N_4$ have been extensively studied for decades,[13, 14] which crystallizes in a porous framework consisting of holes due to large N content.[7] Graphitic $C_3N_4$ has a direct band gap and can be potentially utilized in a wide range of energy and environmental applications, including fuel cells, catalysis, and gas production.[7-9] Likewise, nitrogenated holey grahpene with a $C_2N$ stoichiometry were synthesized by a bottom-up wet-chemical reaction recently.[10] This 2D crystalline $C_2N$ network, with regular holes, has a large electronic band gap of 1.96 eV, making it a promising candidate material for optoelectronics[10] and gas purification.[11, 12] In addition, plenty of C-N materials with different C/N ratios have been theoretically designed via first principle calculations.[15-18]

So far, however, there is rarely any investigation of 2D C-N covalent networks with metallic or better yet nodal-line semimetal (NLSM) features. The NLSMs as new states of quantum matter have been intensively studied recently.[19-31] Particularly, the C based Mackay-Terrones crystal (MTC),[28] $IrF_4$ classes,[32] $PbTaSe_2$,[33] anti-perovskite $Cu_3PdN$,[26, 30] and $Ca_3P_2$ [29] were found to be 3D NLSMs. Attention has also been paid to 2D NLSMs from both experimental research and theoretical design.[20-22, 34-41] The experimental realization of 2D planar $Cu_2Si$ [41] was reported to be a NLSM, in which the nodal lines form two concentric loops centered at Γ point. However, the band touching in $Cu_2Si$ are not rightly lying at the Fermi level and the existence of two nodal loops makes it more challenging for experimental characterization. The first-principle predicted $Hg_3As_2$ [20] and PdS family [21] were only 2D NLSMs in the absence of spin-orbit coupling (SOC) but became gapped in the presence of SOC.[20, 21]

In this work, we propose a novel covalent network consisting of C and N atoms with a $C_9N_4$ stoichiometry from first principle calculation. Most interestingly, it is found to be a 2D NLSM, in contrast to other chemically produced C-N compounds [2, 3, 7, 10] as well as COFs [42, 43] which are all insulating. The nodal line in $C_9N_4$ forms an ideal single loop centered at Γ point without overlapping with any other bands in the momentum space. Mechanistically, this single loop is revealed to be the crossing of two separate sets of bands arising from two sub-lattices, namely the Kagome and Dirac bands. The interpenetration between Kagome and Dirac (honeycomb) lattices proposed recently can lead to different properties, like 2D topological insulator,[44, 45] normal insulator,[46] half metal,[47] Dirac semimetal,[48] and 2D NLSM.[20] In those materials, the sub-lattice sites were occupied by single atoms instead of molecular structural motifs, which are different from our case. The negligible small SOC in $C_9N_4$ is significant for the robustness of nodal line compared with the annihilation in other 2D NLSM containing heavy metals.[20, 21, 40, 41] Moreover, the large chemical potential difference between C and N plays a crucial role in the formation of nodal line in $C_9N_4$, as further confirmed by charge transfer and tight-binding (TB) analysis. Interestingly, there is a new structure of nodal line formed, i.e. "nodal cylinder", in the whole Brillouin zone (BZ) along $\boldsymbol{k_z}$ direction for AA-stacking $C_9N_4$. The gapless linear bands along the high-symmetry path are similar to those in graphene, which implies higher electron mobility. Moreover, the planar 2D structure with large surface-to-volume ratio affords plenty of chemically active sites, potentially useful in sensor applications.[49] Even in the bulk form with different stacking, the system remains metallic, which is different from g-$C_3N_4$.[50] Similar to COFs, we propose a new graphene-type network in the organic-conjugated polymer chemistry. Our results open an avenue for the design of both 2D NLSM and functional covalent organic frameworks.

## Computational methods

The structural optimization and electronic band calculations are performed within the framework of density functional theory (DFT) using Vienna ab-initio simulation package.[51] The Perdew-Burke-Ernzerhof (PBE) [52] functional of generalized gradient approximation is employed. The projector-augmented wave [53] method is used to describe the ion-electron interactions. The HSE06 hybrid functional [54] is used to calculate the band structures to compare with PBE results. The van der Waals interactions are included in the stacked structures by using semiempirical DFT-D3 method.[55] The plane-wave energy cutoff is set to be 500 eV, and the energy convergence criterion in the self-consistency process is $10^{-6}$ eV. A 20 Å length of slab layer is applied along the Z direction to avoid interactions between periodic images. A $\Gamma$ centered $9 \times 9$ grid of **k** points is used to sample the BZ. The phonon spectrum is calculated using a $2\times2$ supercell with Phonopy [56] code. Ab-initio molecular dynamics

(AIMD) simulations with NVT ensemble are conducted to investigate the thermal stability of $C_9N_4$ monolayer. The molecular properties are calculated using Gaussian package [57] at B3LYP level.

**Results and Discussion**

As shown in the right panel of Fig. 1, the proposed covalent network has regular periodic nano-holes, in which C and N atoms are represented by black and blue balls respectively. The hexagonal C rings in the network form a Kagome lattice, which is indicated by dashed green line connecting each center of C rings. Whereas the N constitutes form a honeycomb lattice. Overall, C and N atoms share a 2D hexagonal lattice with the same crystal symmetry ($D_{6h}$) as graphene,[1] where the optimized lattice parameter is 9.64 Å. In the left panel of Fig. 1, a C ring joining with six N atoms is shown to form this new type of network. This building block is also the key component of the precursor HAB, which is utilized to synthesize the crystalline $C_3N$ [2] and $C_2N$ [10] compounds. The unit cell of our proposed C-N network, indicated by red lines in Fig. 1, has 18 C atoms and 8 N atoms resulting in a $C_9N_4$ stoichiometry. It is worth noting that $C_3N$, $C_2N$, and $C_9N_4$ have very similar lattice geometries (Fig. S1 in supplemental information (SI)), implying intimate structural relationships between these monolayer carbon nitrides. The $C_2N$ unit cell is $\sqrt{3}\times\sqrt{3}$ times the $C_3N$ unit cell by removing a C ring; while the $C_9N_4$ unit cell is twice as the $C_3N$ unit cell by removing another C ring. According to the atomic chemical environment and symmetry, there are two kinds of C and N atoms in $C_9N_4$. The optimized C-C and C-N bond lengths are similar to those in $C_2N$,[10] which indicates a strong covalency. The perforated covalent network has rich chemically active edge sites with a lone pair, suggests its potential application in chemical sensors.

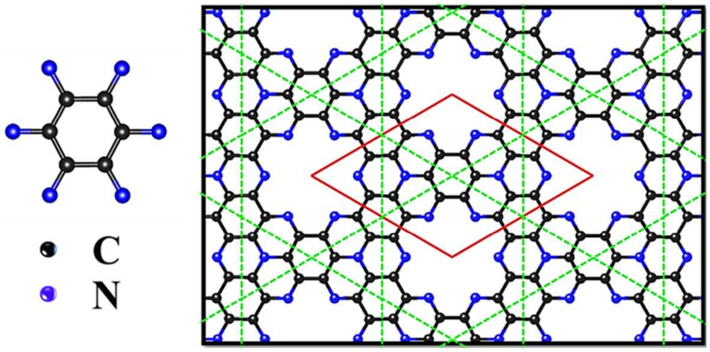

Fig. 1 The left panel shows the building block for $C_9N_4$ covalent network. The right panel presents the $C_9N_4$ crystal structure, where the red line indicates the unit cell. The C rings form a Kagome lattice connected by green dashed lines.

The uniformly distributed N atoms in $C_9N_4$ network have an atomic size comparable with C and a five-electron valence structure, which makes it a favorable option to realize a strong covalent network. The $C_9N_4$ electronic band structure without SOC is shown in Fig. 2 (a). There are two touching points denoted by D1 and D2 in the proximity of Fermi level (set as zero), which implies a semimetallic nature. This unusual feature is apparently different from most previously studied C-N compounds [2, 3, 7, 10] and COFs, [42] which without exception are semiconducting or insulating. To reveal the origin of these two crossing points, the atomic-orbital resolved band structure is plotted in Fig. 2(a), where the sizes of the circles are proportional to the weight of related orbital contributions. It is clear that the two linear crossing bands near the Fermi level stem from the $p_z$ orbitals of C and N atoms. The bands corresponding to the $p_x$ and $p_y$ orbitals lie much deeper below the Fermi level.

Furthermore, there are two sets of distinguishable bands, the Kagome and Dirac bands. The former consists of one flat band and two dispersive bands, arising mainly from the $p_z$ orbitals of C; the latter mainly from the $p_z$ orbitals of both C and N, degenerating at **K** points. The two branches of the linear Kagome and Dirac bands cross with each other at points D1 and D2 along Γ-M and Γ-K paths, respectively. To examine whether there are extra crossing points in the whole BZ, we calculated the band structures throughout the first BZ, as shown in Fig. 2(b). Clearly it shows that there are one concave and one convex energy surface crossing with each other around Γ point, forming a single nodal loop in the BZ. Thus, we identify $C_9N_4$ to be a 2D NLSM. The crossing points D1 and D2 are two points in the same nodal ring as seen in Fig. 2(c). The projected square area for Fig. 2(c) in the first BZ is shown in Fig. 2(d) with red dashed lines.

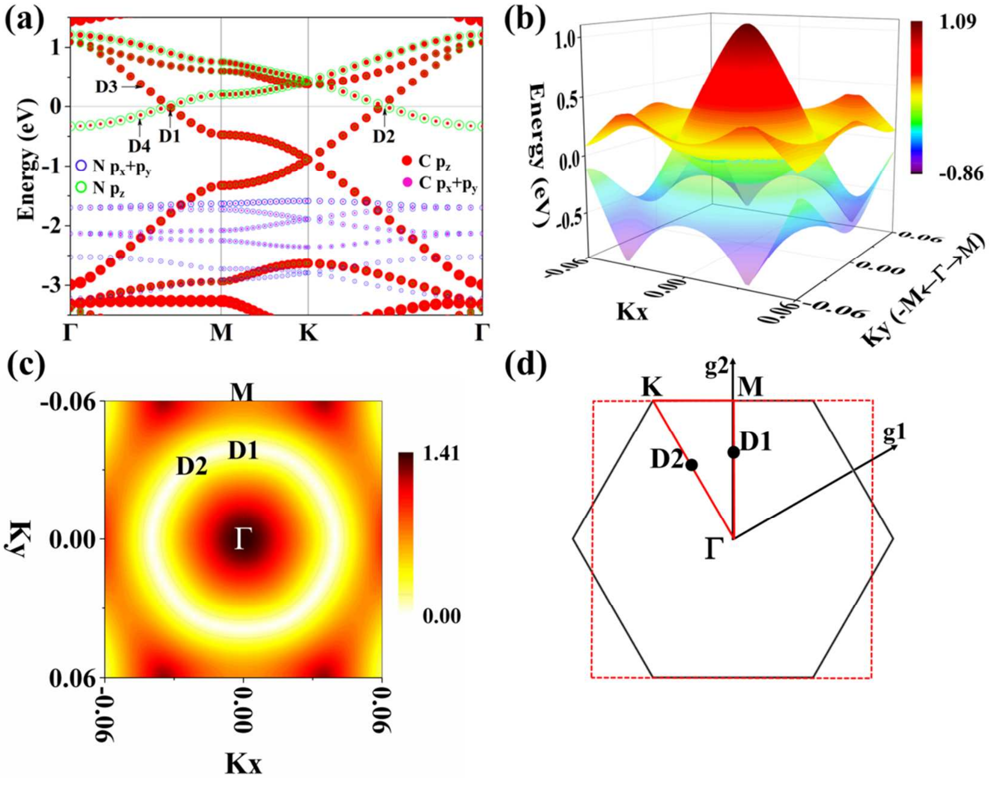

Fig. 2 (a) Projected band structure for $C_9N_4$, where the size of dots is proportional to the weight contributed by different orbitals. (b) 3D band structure of two crossing bands in the vicinity of Fermi level around Γ point. (c) 2D projected Fig. of two crossing bands shown in (b), where the color bar indicates the energy difference between conduction and valence bands at each k point. (d) The 2D BZ for $C_9N_4$, where the dashed square is the projected area for (c).

We note that the gap is generally underestimated by stander DFT calculations, such as for g-$C_3N_4$[14] and orthorhombic $C_3N_4$.[58, 59] Therefore, to confirm the degeneracy of D1 and D2, the hybrid functional calculations are conducted for $C_9N_4$ as shown in Fig. S2. Clearly, the crossing points are remained along Γ-M and Γ-K paths. On the other hand, bands from the $p_x$ and $p_y$ orbitals are located much deeper compared with PBE results. Because the two crossing points are not high-symmetry points, we further calculated the bands around D1 and D2 using HSE functional with a denser k-point mesh. As shown in Fig. S2(c-f), the gap size around D1 and D2 remains essentially zero within the accuracy of numerical calculations, confirming the degeneracy of both D1 and D2.

To compare the states near the two crossing bands, we calculated the charge densities of states at points D3 and D4 close to D1 as shown in Fig. 3(a), which arise from the Kagome and Dirac bands respectively. The D3 state mainly contributed by the $p_z$ orbitals of C exhibits a Kagome distribution, as indicated by the green hexagons. It results from the C rings connecting with each other by an edge hopping path. As shown in Fig. 1, the eight N atoms in the unit cell form a 2×2 honeycomb sub-lattice, however, no band folding feature is observed in the band structure. Nevertheless, the

Dirac bands cross at high symmetric K point, implying a bipartite “superlattice”. For the D4 state, the Dirac bands can be considered as a super-honeycomb lattice consisting of two super-atoms in the unit cell labeled by the blue triangles displayed in Fig. 3(b). Each of the super-atoms has an identical atomic configuration with $C_3$ rotation symmetry without sharing common atoms. It is noted that the two sub-lattices in the Kagome-honeycomb composite lattice proposed before [20] is represented by single atoms instead of a bipartite “superlattice”. Besides, the $p_z$ (on honeycomb sub-lattice) and s (on Kagome sub-lattice) orbitals have opposite parities with respect to the in-plane mirror, which is different from $C_9N_4$ lattice.

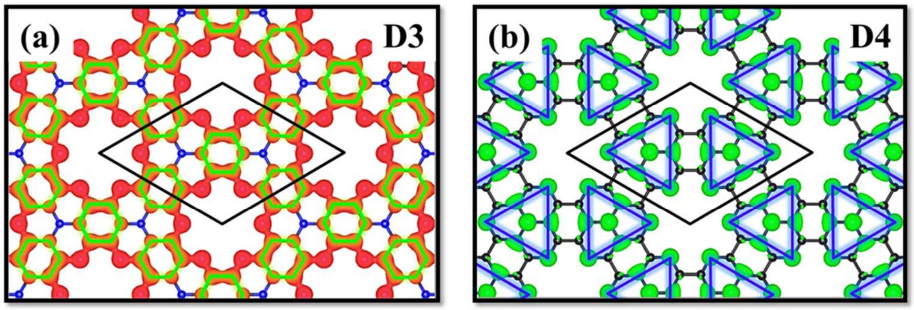

Fig. 3 Charge densities for (a) D3 and (b) D4 states decomposed from Kagome and Dirac bands close to Fermi level respectively. The green hexagons and blue triangles form Kagome and honeycomb lattices respectively.

We note that the nodal line discovered in the previously reported 2D flat monolayer is protected by the in-plane mirror symmetry in the absence of SOC. [20, 41] Meanwhile, the topological index $Z_2$=0, indicating the nodal line in $C_9N_4$ is topologically trivial. In order to better understand the formation of degenerate points along the high-symmetry path K-Γ and Γ-M, we analyze the group symmetry and parity of bands. The point group for 2D $C_9N_4$ is $D_{6h}$, so there are both one vertical mirror plane $\sigma_v$ and one $C_2$ rotation axis existing along K-Γ and Γ-M as shown in Fig. 4(a-b). Along K-Γ and Γ-M, the k-points (except for the end points) from two crossing bands have $C_{2v}$ point group, and the little group have both out-of-plane mirror $\sigma_v$ and $C_2$ rotation symmetry along K-Γ and Γ-M. As shown in Fig. 4(d), the two linear bands along K-Γ and Γ-M belong to two different 1D irreducible representations ($A_2$ and $B_2$). The two bands have opposite parities either with respect to $\sigma_v$ or $C_2$ operation. Therefore, these two crossing bands along K-Γ and Γ-M are decoupled leading to two degenerate points, which are protected by the $\sigma_v$ mirror or $C_2$ rotation symmetry. Such degeneracy along high-symmetry path is similar to the case of graphene,[60] and the main difference is that the touching points in 2D $C_9N_4$ are not at the high-symmetry points.

In addition, two more test calculations were carried out to artificially tune the planar structure to buckled structures to validate the role of $\sigma_v$ mirror and $C_2$ rotation symmetries, as shown in Fig. S3(a, c). The buckled structure in Fig. S3(a) has the $D_{3d}$ point group symmetry. Along K-Γ and Γ-M, the little group has $\sigma_v$ mirror symmetry and $C_2$ operation respectively. And the two crossing bands have opposite parities with respect to $\sigma_v$ and $C_2$ along K-Γ and Γ-M respectively, as shown in Fig. S3(b). The buckled structure in Fig. S3(c) has the $C_{3v}$ point group symmetry. The corresponding band structure in Fig. S3(d) clearly shows there is only one degenerate point along Γ-M protected by $\sigma_v$ mirror. However, the touching point is gapped along K-Γ direction because both the $\sigma_v$ mirror and $C_2$ rotation symmetry are vanished. The gap size (buckling height) is smaller (larger) in comparison with other 2D nodal-line materials containing metal atoms.[21] Interestingly, it is noticed that the degeneracy of Dirac bands at K point is lifted due to the breaking of sub-lattice symmetry in the "bipartite" lattice, resulting in a sizeable gap $E_D$ shown in Fig. S3(d), which is consistent with the chemical potential difference of two super-atoms occupying the two sub-lattices respectively.

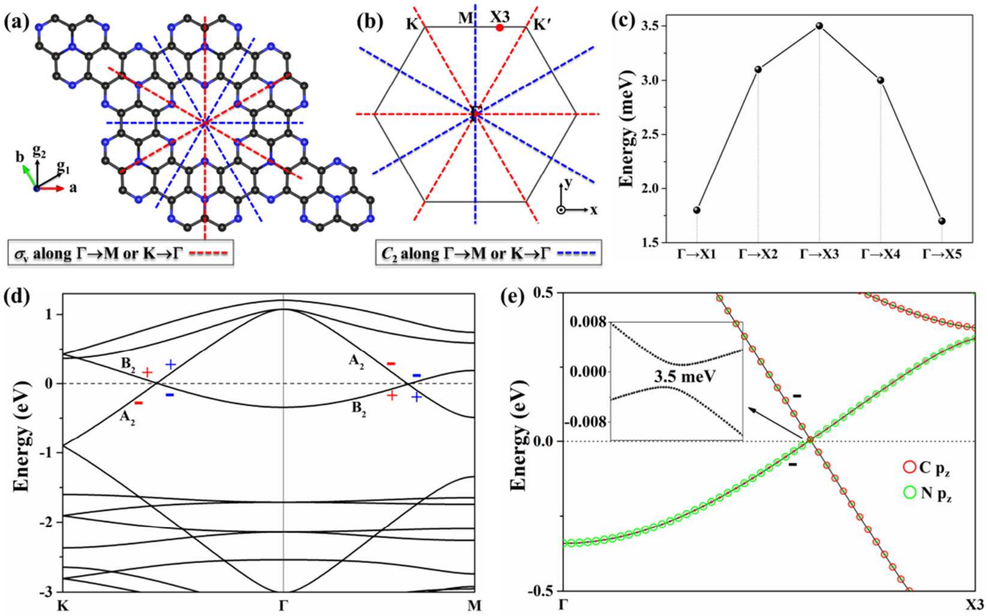

Fig. 4 (a) The 2D crystal structure and (b) BZ for $C_9N_4$ respectively, where the red and blue dashed lines indicate the out-of-plane $\sigma_v$ mirror plane and $C_2$ rotation axis along K-Γ-M. (c) Gap size obtained along Γ-Xi (i=1, 2 , 3, 4, 5) (d) Band structure for $C_9N_4$ along K-Γ-M, where the "+" and "-" symbols indicate the parities of crossing bands with respect to $\sigma_v$ mirror plane or $C_2$ rotation axis in the same color. (e) Band structure for $C_9N_4$ along Γ-X3, where the "-" symbol is the parities of crossing bands with respect to horizontal mirror plane. The green and red circles are proportional to the contributions from $p_z$ orbitals of N and C respectively.

In addition to the degeneracy along high-symmetry paths, we also examined other touching points in the nodal ring (Fig. 2(c)). The band structure shown in Fig. 4(e) is calculated along Γ-X3 path. The point X3 is in the middle of M-K′ path shown in Fig. 4(b). The magnified band in Fig. 4(e) shows that there is a tiny gap (3.5 meV) opened at the nodal point along Γ-X3 path, which can be understood by symmetry analysis. The k-points along Γ-X3 (except for the end points) have the $C_s$ point group symmetry. The little group has one horizontal mirror plane $\sigma_h$. Because the crossing bands are all contributed by $p_z$ orbitals, they become coupled with the same mirror odd parities with respect to $\sigma_h$. This gives rise to the tiny gap as formed. The tiny gaps are also found along Γ-Xi (i=1, 2, 3, 4) as shown in Fig 4(c). Their sizes are all checked within denser k-points calculated at PBE level. The 5 Xi (i=1, 2, 3, 4, 5) k-points divide M-K′ path equally. From Fig. 4(c), it is further shown that the gap sizes along other four paths are symmetrical with respective to those along Γ-X3. Given the symmetry of k-points in the first BZ, it is known there are total 12 exact degenerate points in the nodal ring. The largest gap size is 3.5 meV along the nodal ring by PBE calculation, which is confirmed to be in the same order of magnitude about 3 meV by HSE calculation. Given this negligible gap size induced by weak coupling of $p_z$ orbitals, the 2D $C_9N_4$ can still be considered as a NLSM.

The above calculations are performed without SOC, so it is natural to ask weather this nodal line in $C_9N_4$ is immune to SOC. It is found that the SOC strength (even artificially tuning larger) induced gap size is very tiny shown in Fig. S4. Hence, the nodal line in $C_9N_4$ is robust against the intrinsic SOC effect in C and N. Therefore, all three factors, the protection of multiple crystal symmetries, negligible SOC and negligible gap size induced by $p_z$-orbital coupling, contribute together to make the 2D

$C_9N_4$ an ideal semimetallic property.

To better understand the effect of chemical potential difference on the formation of nodal loop in $C_9N_4$, a TB analysis is shown below. Due to the fact that only the $p_z$ orbitals of both C and N atoms contribute to the states close to Fermi level, we can construct a TB model with only the $p_z$ orbitals,

$$\hat{H} = \sum_i \varepsilon_i a_i^+ a_i + \sum_{i \neq j} t_{ij} a_i^+ a_j \quad (1)$$

where $a^+$ and $a$ are electron creation and annihilation operators, $i$, $j$ are the sites of atoms in the unit cell, $t_{ij}$ is the hopping energy between $p_z$ orbitals at site $i$ and $j$, $\varepsilon$ is the on-site energy. We only consider the nearest-neighbor hopping without SOC. As mentioned above, there are two different C and N atoms according to the symmetry and chemical environment. Consequently, four interatomic hopping terms are introduced in the TB model, as shown in Fig. 5(a). The red and gray balls represent N and C atoms respectively, whose size denotes the charge value based on the grid-dependent Bader charge analysis.[61] The calculated results indicate that each N(1) (N(2)) atom gains 1.1 (1.2) electrons, while each C(1) (C(2)) atom loses 0.6 (0.3) electrons. Apparently, the charge transfer happens from C to N due to their electronegativity difference. The TB band structure is calculated to fit the DFT results as shown in Fig. 5(b), where only the five bands comprising three Kagome and two Dirac bands are plotted. Table 1 lists the corresponding fitting parameters of hopping and on-site energies. The bond lengths between different atoms, for which the hopping integrals are indicated from $t_1$ to $t_4$ (Fig. 5(a)), are 1.39, 1.46, 1.42, and 1.34 Å, respectively. The hopping integrals are about the same since the bond lengths are close to each. However, it is obvious that the on-site energy difference between C and N is rather large. Interestingly, we found that the superposition of the three Kagome bands and the two Dirac bands are mainly attributed to the large on-site energy of N(2) atoms. As illustrated in Fig. 5(c-d), the Dirac point shifted upwards above the flat Kagome band when the on-site energy of N(2) atom is decreased, while the other TB parameters are fixed. Moreover, the width and dispersion of the three Kagome bands are barely affected, and only the Dirac bands are influenced by the change of on-site energy of two super-atoms in the unit cell. In particular, when on-site energy of N(2) atoms changes to -1 eV, the linear band crossing disappears as shown from Fig. 5(d). Therefore, the linear crossing is mainly determined by the larger on-site energy of N(2) atoms. Also seen from Fig. 5 (b), the band structures obtained by TB and DFT calculations agree well except the flat band. From DFT results (Fig. 2(a) and Fig. 5(b)), the flat band is pulled down to **K** point and becomes slightly dispersive, which is different from the perfect flat band in TB results. This is because in TB calculation, only nearest-neighbor hopping terms are considered. In fact, such localized flat band in Kagome lattice is known to become dispersive when introducing second nearest neighbor hopping interactions.[62] Furthermore, in DFT calculations, the linear-crossing bands are contributed by both $p_z$ orbitals of honeycomb and Kagome lattices. Hence, there are hybridizations between the Dirac and Kagome bands. Nevertheless the main feature of linear crossing pertained to the two sets of dispersive bands is captured by the TB model.

To further understand the formation of the intrinsic nodal ring in our 2D covalent system, the properties of molecular orbitals (MOs) for single super atom ($C_9N_4$) and whole unit cell ($(C_9N_4)_2$) are calculated with Gaussian package. As seen from Fig. S5, the unoccupied MOs from Dirac bands and partially filled MOs from Kagome bands determine the electron filling from the DFT results, i.e., nearly unfilled Dirac band and 2/3 filled Kagome bands. Moreover, the interaction between the wider dispersive Kagome bands and the narrower Dirac bands leads to a crossover giving rise to the degenerate nodal loop. More details are shown in the SI.

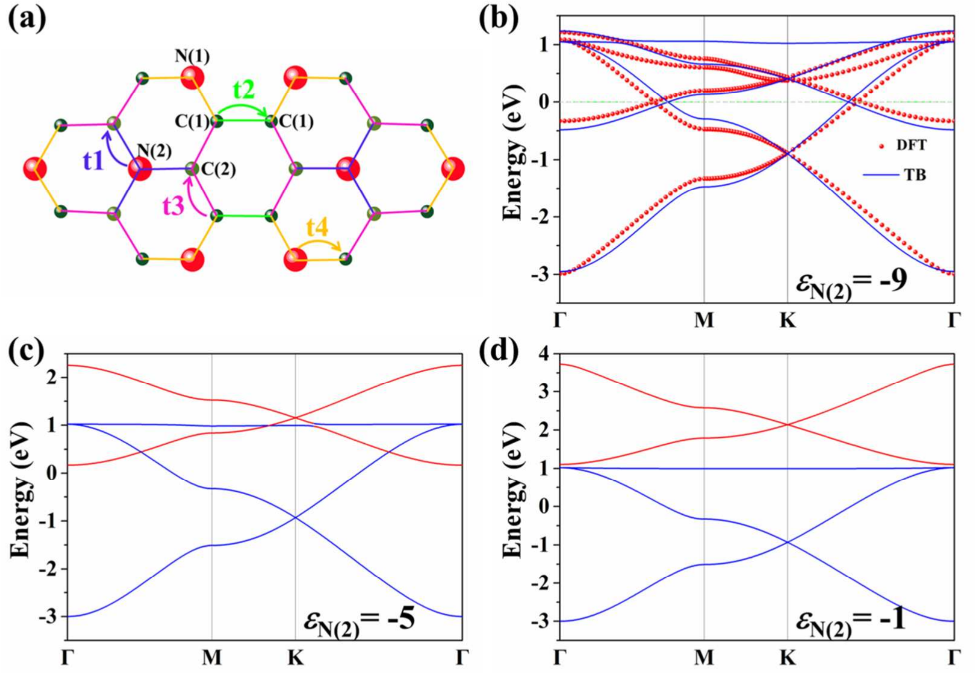

Fig. 5 (a) Bader charge analysis for $C_9N_4$ unit cell. The red and gray balls represent N and C atoms. The sizes of balls imply the charge values. (b) Band structure for $C_9N_4$ simulated by TB analysis (blue solid line) compared with DFT results (red dashed line). (c) Band structure for $C_9N_4$ simulated by TB analysis with $\varepsilon_{N(2)}$ = -5 eV and (d) $\varepsilon_{N(2)}$ = -1 eV, while other parameters are fixed.

Table 1. Values of hopping and on-site energy (unit is electron-volt) applied in TB analysis.

| | $t_1$ | $t_2$ | $t_3$ | $t_4$ |
|---|---|---|---|---|
| $p_zp_z$ | 4.0 | 3.8 | 3.9 | 4.1 |
| on-site energy | $\varepsilon_{N(1)}$=-5; | $\varepsilon_{N(2)}$=-9; | $\varepsilon_{C(1)}$=0.8; | $\varepsilon_{C(2)}$=0.0 |

The relative energy stability among different stacking configurations is investigated. We started with the AA-stacking, which has an optimized interlayer length of 3.45 Å, typical for a van der Waals (vdW) interaction. As shown in the inset of Fig. S6(a), then the top layer is shifted along one of the shorter diagonal directions until reaching half of the lattice constant of AA-$C_9N_4$ to assume an AB-stacking. The AB-stacking is found energetically more preferable by 38 meV/atom. This implies that the AA-stacking is metastable but may still be energetically accessible as seen in other 2D materials.

Due to the missing of some crystal symmetries along M-Γ-K in AB-stacking $C_9N_4$, some crossing points become gapped as shown in Fig. S6(b). Whereas it remains gapless along M-Γ-K in AA-stacking $C_9N_4$, in which the crystal symmetries are preserved as in 2D $C_9N_4$. We note that neither AA nor AB-stacking $C_9N_4$ is a semiconductor, which is different from the AA and AB-stacking g-$C_3N_4$.[50]

The band structure for AA-stacking $C_9N_4$ is shown in Fig. S7. Interestingly, the two linear crossing points shift downwards from $\boldsymbol{k_z}$=0 to $\boldsymbol{k_z}$=0.5 plane. Therefore, the crossing points will form a new structure of nodal line, i.e. “nodal cylinder” along $\boldsymbol{k_z}$ direction in the whole BZ, which is different from other simple nodal-line semimetals, [23, 24, 27, 63, 64] nodal-chain metals, [32] nodal-net semimetals, [26, 30] nodal-link semimetals, [19, 65, 66] and nodal-knot semimetals. [67] As shown in Fig. S8, there are two nodal lines along $\boldsymbol{k}_z$ direction on $\boldsymbol{k}_y$=0 plane, which further confirm the existence of nodal cylinder. Therefore, the preserved crystal symmetry and weak vdW interactions ensure the existence of nodal cylinder in AA-stacking $C_9N_4$.

Finally, to evaluate the stability of such a new type of C-N network, we compare the energy of monolayer $C_9N_4$ with pristine graphene, and other experimentally realized 2D C-N materials ($C_3N$, $C_2N$, and g-$C_3N_4$). The lower energy shown in Fig. S9 for monolayer $C_9N_4$ partially confirms its higher stability. The result is in agreement with the previously studied 2D $C_3N$, $C_2N$, and g-$C_3N_4$.[4] However, such comparison of total energy is insufficient because of their different stoichiometry. Therefore, we further calculate the formation energies of different C-N compounds using the chemical potentials from two known reagents, graphene and molecular nitrogen, according to the formula: $E_f=[E_{tot}(C_pN_q)-p/2\times E_{tot}(\text{graphene})-q/2\times E_{tot}(N_2)]/(p+q)$, where p and q are the number of C and N atoms in the unit cell, respectively; $E_{tot}(C_pN_q)$, $E_{tot}(\text{graphene})$, and $E_{tot}(N_2)$ are the total energy of 2D C-N compounds, graphene, and $N_2$, respectively. The formation energies in Fig. S9 show similar trends as the total energies, suggesting the energetic stability of 2D $C_9N_4$.

Moreover, the phonon and AIMD computations are performed. There is no soft mode observed in phonon spectrum (Fig. S10), implying the dynamic stability. Further calculation is conducted to study the thermal stability at room temperature (300 K) by performing AIMD simulations. The results (Fig. S10 (b-c)) indicate that there is no structural decomposition observed at 300 K after 10 ps. We also calculated the linear elastic properties from the strain-energy relationship by DFT calculations to investigate the mechanical stability. Due to symmetry, the 2D hexagonal crystal has two independent elastic constants $C_{11}$ and $C_{12}$. [68] The computed values of $C_{11}$ and $C_{12}$ are 208 and 49 N/m respectively, which fulfill the Born stability criteria [69] ($C_{11}>0$, $C_{11}>|C_{12}|$). The other elastic quantities, such as Poisson's ratio and Young's moduli can be evaluated by the following equations,[70, 71]

$$v = \frac{C_{12}}{C_{11}}, \qquad E = \frac{C_{11}^2 - C_{12}^2}{C_{11}} \tag{2}$$

The obtained in-plane Poisson's ratio (Young's moduli) is 0.24 (196 N/m), which is larger (smaller) than those of graphene and $C_3N$.[71] Therefore, our calculations from phonon dispersion, AIMD simulations, and mechanical elastic properties consistently suggest that the $C_9N_4$ network has rather high thermodynamic and mechanical stabilities. All the evidence suggests the synthesis of 2D $C_9N_4$ under ambient conditions is possible. We propose $C_9N_4$ could be possibly synthesized utilizing similar synthesis processes applied for g-$C_3N_4$,[7] $C_2N$,[10, 72] $C_3N$,[2, 3] and COFs.[42]

## Conclusions

In summary, a new 2D NLSM is predicted using first-principle calculations, which enriches the realm of both COFs and C-N compounds. This novel monolayer with a $C_9N_4$ stoichiometry possesses a nodal line centered at Γ point in the k-space forming a closed loop. This new feature is rarely found in other C-N compounds and

COFs. The touching points along K-Γ-M are protected by the out-of-plane mirror and $C_2$ rotation symmetry. The nodal line is contributed by the $p_z$ orbitals of C and N, as further confirmed by the single orbital TB analysis. From the analysis on charge transfer and TB results, it is found that the C and N have a large on-site energy difference, particularly, the much larger on-site energy of N(2) atoms plays a significant role in forming such linear crossing at Fermi level. The single nodal loop in $C_9N_4$ is intrinsically immune to the SOC effect due to the super light constituent elements, C and N, which shows an ideal semimetallic properties compared with heavy metal-involved NLSM. Interestingly, a nodal cylinder forms in the AA-stacking $C_9N_4$ along $\boldsymbol{k}_\mathbf{z}$ direction in the whole BZ. The thermodynamic and mechanical stabilities of 2D $C_9N_4$ are guaranteed from our calculations. Our results not only shed light on searching a new kind of 2D C-N material, but also suggest a novel member among COFs with unusual semimetallic properties.

## Conflicts of interest

There are no conflicts of interest to declare.

## Acknowledgements

X.N. acknowledges the financial support from the Recruitment Program of Global Young Experts of China and Sichuan one thousand Talents Plan. F.L. acknowledges the support from US-DOE (Grant No. DE-FG02-04ER46148). H.C. acknowledges the financial support from the Graduate School of UESTC. S.Z. is supported by the National Postdoctoral Program for Innovative Talents of China (BX201600091) and the Funding from China Postdoctoral Science Foundation

(2017M610858). The computational resources are supported by CHPC at the University of Utah and National SuperComputer Center in Tianjing, China.

## References

1. K. S. Novoselov, A. K. Geim, S. V. Morozov, D. Jiang, Y. Zhang, S. V. Dubonos, I. V. Grigorieva and A. A. Firsov, *Science*, 2004, **306**, 666-669.
2. J. Mahmood, E. K. Lee, M. Jung, D. Shin, H. J. Choi, J. M. Seo, S. M. Jung, D. Kim, F. Li, M. S. Lah, N. Park, H. J. Shin, J. H. Oh and J. B. Baek, *Proc. Natl. Acad. Sci. U.S.A.*, 2016, **113**, 7414-7419.
3. S. W. Yang, W. Li, C. C. Ye, G. Wang, H. Tian, C. Zhu, P. He, G. Q. Ding, X. M. Xie, Y. Liu, Y. Lifshitz, S. T. Lee, Z. H. Kang and M. H. Jiang, *Adv. Mater.*, 2017, **29**, 1605625.
4. B. Mortazavi, *Carbon*, 2017, **118**, 25-34.
5. M. Makaremi, B. Mortazavi and C. V. Singh, *J. Phys. Chem. C*, 2017, **121**, 18575-18583.
6. W. F. Li, X. Dai, J. Morrone, G. Zhang and R. H. Zhou, *Nanoscale*, 2017, **9**, 12025-12031.
7. X. C. Wang, K. Maeda, A. Thomas, K. Takanabe, G. Xin, J. M. Carlsson, K. Domen and M. Antonietti, *Nat. Mater.*, 2009, **8**, 76-80.
8. Y. Zheng, J. Liu, J. Liang, M. Jaroniec and S. Z. Qiao, *Energy Environ. Sci.*, 2012, **5**, 6717-6731.
9. Y. Zheng, Y. Jiao, J. Chen, J. Liu, J. Liang, A. Du, W. M. Zhang, Z. H. Zhu, S. C. Smith, M. Jaroniec, G. Q. Lu and S. Z. Qiao, *J. Am. Chem. Soc.*, 2011, **133**, 20116-20119.
10. J. Mahmood, E. K. Lee, M. Jung, D. Shin, I. Y. Jeon, S. M. Jung, H. J. Choi, J. M. Seo, S. Y. Bae, S. D. Sohn, N. Park, J. H. Oh, H. J. Shin and J. B. Baek, *Nat. Commun.*, 2015, **6**, 6486.
11. B. Xu, H. Xiang, Q. Wei, J. Q. Liu, Y. D. Xia, J. Yin and Z. G. Liu, *Phys. Chem. Chem. Phys.*, 2015, **17**, 15115-15118.
12. F. Li, Y. Y. Qu and M. W. Zhao, *Carbon*, 2015, **95**, 51-57.
13. A. Thomas, A. Fischer, F. Goettmann, M. Antonietti, J. O. Muller, R. Schlogl and J. M. Carlsson, *J. Mater. Chem.*, 2008, **18**, 4893-4908.
14. J. Ortega and O. F. Sankey, *Phys. Rev. B*, 1995, **51**, 2624-2627.
15. S. H. Zhang, J. Zhou, Q. Wang and P. Jena, *J. Phys. Chem. C*, 2016, **120**, 3993-3998.
16. Y. X. Feng, X. L. Yao, M. Wang, Z. P. Hu, X. G. Luo, H. T. Wang and L. X. Zhang, *J. Chem. Phys.*, 2013, **138**, 164706.
17. J. N. Hart, F. Claeyssens, N. L. Allan and P. W. May, *Phys. Rev. B*, 2009, **80**, 174111.
18. H. J. Xiang, B. Huang, Z. Y. Li, S. H. Wei, J. L. Yang and X. G. Gong, *Phys. Rev. X*, 2012, **2**, 011003.
19. Z. B. Yan, R. Bi, H. T. Shen, L. Lu, S. C. Zhang and Z. Wang, *Phys. Rev. B*, 2017, **96**, 041103.
20. J. L. Lu, W. Luo, X. Y. Li, S. Q. Yang, J. X. Cao, X. G. Gong and H. J. Xiang, *Chin. Phys. Lett.*, 2017, **34**, 057302.
21. Y. J. Jin, R. Wang, J. Z. Zhao, Y. P. Du, C. D. Zheng, L. Y. Gan, J. F. Liu, H. Xu and S. Y. Tong, *Nanoscale*, 2017, **9**, 13112-13118.
22. S. Barati and S. H. Abedinpour, *Phys. Rev. B*, 2017, **96**, 155150.

23. A. A. Burkov, M. D. Hook and L. Balents, *Phys. Rev. B*, 2011, **84**, 235126.
24. H. Q. Huang, K. H. Jin and F. Liu, *Phys. Rev. B*, 2017, **96**, 115106
25. H. Q. Huang and F. Liu, *Phys. Rev. B*, 2017, **95**, 201101.
26. Y. Kim, B. J. Wieder, C. L. Kane and A. M. Rappe, *Phys. Rev. Lett.*, 2015, **115**, 036806.
27. R. Yu, Z. Fang, X. Dai and H. M. Weng, *Front. Phys.*, 2017, **12**, 127202.
28. H. M. Weng, Y. Y. Liang, Q. N. Xu, R. Yu, Z. Fang, X. Dai and Y. Kawazoe, *Phys. Rev. B*, 2015, **92**, 045108.
29. Y. H. Chan, C. K. Chiu, M. Y. Chou and A. P. Schnyder, *Phys. Rev. B*, 2016, **93**, 205132.
30. R. Yu, H. M. Weng, Z. Fang, X. Dai and X. Hu, *Phys. Rev. Lett.*, 2015, **115**, 036807.
31. Z. Liu, H. Wang, Z. F. Wang, J. Yang and F. Liu, *Phys. Rev. B*, 2018, **97**, 155138.
32. T. Bzdusek, Q. S. Wu, A. Ruegg, M. Sigrist and A. A. Soluyanov, *Nature*, 2016, **538**, 75-78.
33. G. Bian, T. R. Chang, R. Sankar, S. Y. Xu, H. Zheng, T. Neupert, C. K. Chiu, S. M. Huang, G. Q. Chang, I. Belopolski, D. S. Sanchez, M. Neupane, N. Alidoust, C. Liu, B. K. Wang, C. C. Lee, H. T. Jeng, C. L. Zhang, Z. J. Yuan, S. Jia, A. Bansil, F. C. Chou, H. Lin and M. Z. Hasan, *Nat. Commun.*, 2016, **7**, 10556.
34. C. Niu, P. M. Buh, H. Zhang, G. Bihlmayer, D. Wortmann, S. Blügel and Y. Mokrousov, 2017, arXiv:1703.05540.
35. R.-W. Zhang, C.-C. Liu, D.-S. Ma and Y. Yao, 2017, arXiv:1710.06267.
36. P. Zhou, Z. S. Ma and L. Z. Sun, *J. Mater. Chem. C*, 2018, **6**, 1206-1214.
37. H. H. Zhang, Y. Xie, Z. W. Zhang, C. Y. Zhong, Y. F. Li, Z. F. Chen and Y. P. Chen, *J. Phys. Chem. Lett.*, 2017, **8**, 1707-1713.
38. B. Yang, X. M. Zhang and M. W. Zhao, *Nanoscale*, 2017, **9**, 8740-8746.
39. L. H. Li and M. A. N. Araujo, *Phys. Rev. B*, 2016, **94**, 165117.
40. C. W. Niu, P. M. Buhl, G. Bihlmayer, D. Wortmann, Y. Dai, S. Blugel and Y. Mokrousov, *Phys. Rev. B*, 2017, **95**, 235138.
41. B. J. Feng, B. T. Fu, S. Kasamatsu, S. Ito, P. Cheng, C. C. Liu, Y. Feng, S. L. Wu, S. K. Mahatha, P. Sheverdyaeva, P. Moras, M. Arita, O. Sugino, T. C. Chiang, K. Shimada, K. Miyamoto, T. Okuda, K. H. Wu, L. Chen, Y. G. Yao and I. Matsuda, *Nat. Commun.*, 2017, **8**, 1007.
42. C. S. Diercks and O. M. Yaghi, *Science*, 2017, **355**, 923.
43. H. Y. Chen, K. H. Jin, H. Guo, B. J. Wang, A. O. Govorov, X. B. Niu and Z. M. Wang, *Carbon*, 2018, **126**, 480-488.
44. H. P. Wang, W. Luo and H. J. Xiang, *Phys. Rev. B*, 2017, **95**, 125430.
45. S. J. Zhang, C. W. Zhang, S. F. Zhang, W. X. Ji, P. Li, P. J. Wang, S. S. Li and S. S. Yan, *Phys. Rev. B*, 2017, **96**, 205433.
46. T. T. Song, M. Yang, J. W. Chai, M. Callsen, J. Zhou, T. Yang, Z. Zhang, J. S. Pan, D. Z. Chi, Y. P. Feng and S. J. Wang, *Sci. Rep.*, 2016, **6**, 29221.
47. W. X. Ji, B. M. Zhang, S. F. Zhang, C. W. Zhang, M. Ding, P. Li and P. J. Wang, *J. Mater. Chem. C*, 2017, **5**, 8504-8508.
48. B. Wang, S. J. Yuan, Y. H. Li, L. Shi and J. L. Wang, *Nanoscale*, 2017, **9**, 5577-5582.
49. H. J. Yoon, D. H. Jun, J. H. Yang, Z. X. Zhou, S. S. Yang and M. M. C. Cheng, *Sens. Actuator B-Chem.*, 2011, **157**, 310-313.
50. A. H. Reshak, S. A. Khan and S. Auluck, *RSC Adv.*, 2014, **4**, 6957-6964.
51. G. Kresse and J. Furthmuller, *Comput. Mater. Sci.*, 1996, **6**, 15-50.

52. J. P. Perdew, K. Burke and M. Ernzerhof, *Phys. Rev. Lett.*, 1996, **77**, 3865-3868.
53. P. E. Blochl, *Phys. Rev. B*, 1994, **50**, 17953-17979.
54. O. A. Vydrov, J. Heyd, A. V. Krukau and G. E. Scuseria, *J. Chem. Phys.*, 2006, **125**, 074106.
55. S. Grimme, J. Antony, S. Ehrlich and H. Krieg, *J. Chem. Phys.*, 2010, **132**, 154104.
56. A. Togo and I. Tanaka, *Scripta Mater.*, 2015, **108**, 1-5.
57. M. J. Frisch, G. W. Trucks, H. B. Schlegel, G. E. Scuseria, M. A. Robb, J. R. Cheeseman, G. Scalmani, V. Barone, G. A. Petersson, H. Nakatsuji, X. Li, M. Caricato, A. V. Marenich, J. Bloino, B. G. Janesko, R. Gomperts, B. Mennucci, H. P. Hratchian, J. V. Ortiz, A. F. Izmaylov, J. L. Sonnenberg, Williams, F. Ding, F. Lipparini, F. Egidi, J. Goings, B. Peng, A. Petrone, T. Henderson, D. Ranasinghe, V. G. Zakrzewski, J. Gao, N. Rega, G. Zheng, W. Liang, M. Hada, M. Ehara, K. Toyota, R. Fukuda, J. Hasegawa, M. Ishida, T. Nakajima, Y. Honda, O. Kitao, H. Nakai, T. Vreven, K. Throssell, J. A. Montgomery Jr., J. E. Peralta, F. Ogliaro, M. J. Bearpark, J. J. Heyd, E. N. Brothers, K. N. Kudin, V. N. Staroverov, T. A. Keith, R. Kobayashi, J. Normand, K. Raghavachari, A. P. Rendell, J. C. Burant, S. S. Iyengar, J. Tomasi, M. Cossi, J. M. Millam, M. Klene, C. Adamo, R. Cammi, J. W. Ochterski, R. L. Martin, K. Morokuma, O. Farkas, J. B. Foresman and D. J. Fox, *Gaussian 16*, Wallingford, CT, 2016.
58. Y. Xu and S. P. Gao, *Int. J. Hydro. Energy*, 2012, **37**, 11072-11080.
59. M. Mattesini, S. F. Matar and J. Etourneau, *J. Mater. Chem.*, 2000, **10**, 709-713.
60. S. Minami, I. Sugita, R. Tomita, H. Oshima and M. Saito, *Jpn. J. Appl. Phys.*, 2017, **56**, 105102.
61. W. Tang, E. Sanville and G. Henkelman, *J. Phys.: Condens. Matter*, 2009, **21**, 084204.
62. H. Takeda, T. Takashima and K. Yoshino, *J. Phys.: Condens. Matter*, 2004, **16**, 6317-6324.
63. M. Phillips and V. Aji, *Phys. Rev. B*, 2014, **90**, 115111.
64. C. Fang, H. M. Weng, X. Dai and Z. Fang, *Chin. Phys. B*, 2016, **25**.
65. W. Chen, H. Z. Lu and J. M. Hou, *Phys. Rev. B*, 2017, **96**, 041102.
66. P. Y. Chang and C. H. Yee, *Phys. Rev. B*, 2017, **96**, 081114.
67. R. Bi, Z. B. Yan, L. Lu and Z. Wang, *Phys. Rev. B*, 2017, **96**, 201305.
68. K. H. Michel and B. Verberck, *Phys. Rev. B*, 2009, **80**, 224301.
69. F. Mouhat and F. X. Coudert, *Phys. Rev. B*, 2014, **90**, 224104.
70. Q. Wei and X. H. Peng, *Appl. Phys. Lett.*, 2014, **104**, 251915.
71. X. D. Zhou, W. X. Feng, S. Guan, B. T. Fu, W. Y. Su and Y. G. Yao, *J. Mater. Res.*, 2017, **32**, 2993-3001.
72. J. Mahmood, F. Li, S. M. Jung, M. S. Okyay, I. Ahmad, S. J. Kim, N. Park, H. Y. Jeong and J. B. Baek, *Nat. Nanotechnol.*, 2017, **12**, 441-446.

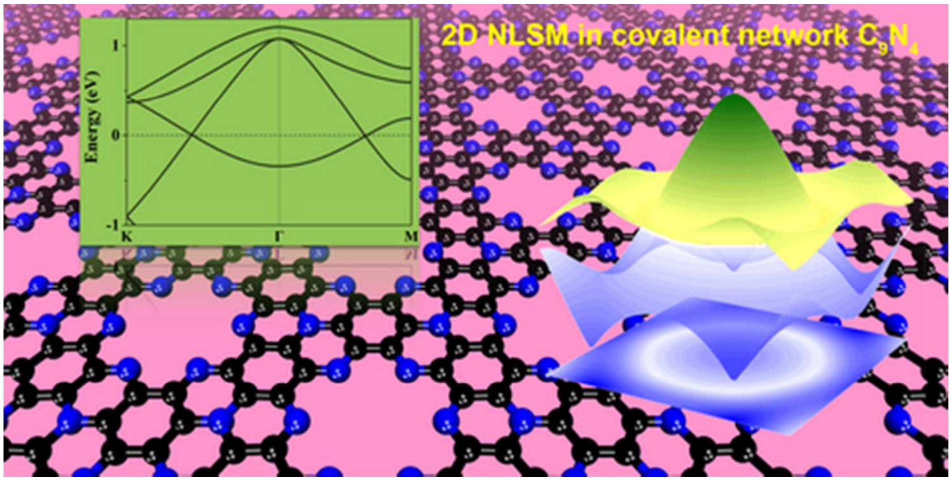

Graphical Abstract

39x19mm (300 x 300 DPI)